



Engineering Notes

Initial Orbit Determination from Bearing and Range-Rate Measurements Using the Orbital Hodograph

John A. Christian* and William E. Parker†

Rensselaer Polytechnic Institute, Troy, New York 12180

<https://doi.org/10.2514/1.G005433>

I. Introduction

SOME of the earliest work in astrodynamics was motivated by efforts to characterize the orbital motion of observed bodies in space from limited measurements. The classical methods developed by Laplace [1], Gauss [2], and Gibbs [3] made use of the measurements that were available from the equipment of their time. Thus, these early methods primarily made use of angles and positions that could be manually observed through optical telescopes.

In the twentieth century, improved Earth-based sensing technologies (e.g., radar [4]) were developed to track space objects. Additionally, humans transitioned from only observing the orbits of natural celestial objects to also observing crewed and uncrewed artificial satellites. Unlike natural satellites, human-built spacecraft are capable of collecting in situ measurements (e.g., radio frequency [RF] observables [5,6], images [7,8], x-ray pulsar signals [9]). These new types of measurements (both Earth-based and in situ) motivated new classes of orbit determination problems that are now familiar to the practicing astrodynamist [10,11]. Recently, a novel class of orbit determination has been suggested where only velocity measurements are available [12,13]—a scenario most plausible with the StarNAV concept [14–16]. This work on velocity-based initial orbit determination (IOD) and StarNAV has renewed interest in the utility of Hamilton's orbital hodograph as a tool for navigation analysis, and serves as the motivation for the present study.

In this paper, the authors propose efficient IOD solutions for a spacecraft obtaining concurrent range-rate (or altitude-rate) measurements and bearings to the central body. Such measurements could be achieved in Earth orbit by a spacecraft with an altimeter (for range rate) and an Earth sensor (for bearing to central body). Bearing to the Earth's center could also be provided using OPNAV methods [7,8]. A similar sensor setup could be used to obtain range-rate and bearing to the central body for the Moon, Mars, or other bodies within the solar system. Additionally, a spacecraft in heliocentric orbit may obtain bearing to the central body with a sun sensor and range-rate using Doppler shift of the solar spectra. While there are challenges in using Doppler shift of solar spectra for navigation [14,17], it has been studied in the past [18–20] and may be possible with future technological advances.

Received 1 June 2020; revision received 5 September 2020; accepted for publication 18 October 2020; published online 23 November 2020. Copyright © 2020 by the authors. Published by the American Institute of Aeronautics and Astronautics, Inc., with permission. All requests for copying and permission to reprint should be submitted to CCC at www.copyright.com; employ the eISSN 1533-3884 to initiate your request. See also AIAA Rights and Permissions www.aiaa.org/randp.

*Associate Professor, Department of Mechanical, Aerospace, and Nuclear Engineering. Associate Fellow AIAA.

†Undergraduate Student, Department of Mechanical, Aerospace, and Nuclear Engineering; currently Graduate Student, Aeronautics and Astronautics, Massachusetts Institute of Technology, Cambridge, MA.

Regardless of the specific sensing technologies, study of IOD from bearing and range-rate measurements presents an interesting problem—especially when explored within the context of the orbital hodograph. Recognizing that the hodograph may be an obscure tool to many readers, Sec. II develops important hodograph properties from familiar relations for two-body motion. Then, Secs. III and IV describe various methods for IOD with the hodograph. Example numerical results are shown in Sec. V. Throughout, care is taken to develop compact expressions written explicitly in terms of the key hodograph parameters (c and R). Many of these expressions are generically useful and not widely known—indeed, some of these relations have not been seen by the authors in any other text describing the hodograph.

II. Orbital Hodograph

The locus of points traced out by the tip of a trajectory's velocity vector while keeping the tail fixed at the origin is generally called a *hodograph*—a concept first introduced by Hamilton in 1847 [21]. In this seminal work, Hamilton demonstrated that the orbital hodograph is a perfect circle for every two-body orbit, regardless of the shape of the orbit (circle, ellipse, parabola, hyperbola). The circular shape of the orbital hodograph has been rediscovered many times since Hamilton [22], and the authors make no claim of originality regarding either the hodograph concept or its shape. Despite its long history, however, the hodograph is not part of a typical astrodynamics education in the United States. Indeed, it receives no detailed treatment in many of the most popular instructional texts (e.g., [23–26]) and only brief discussion in others [27]—though detailed treatment does occur in a few obscure texts [28]. Consequently, its existence and properties are not widely known among contemporary practitioners. What follows, therefore, is the authors' approach for developing the hodograph using conventions familiar to the modern astrodynamist.

Consider the case of a small body (e.g., spacecraft) orbiting a large central body (e.g., Earth). In this case, the application of Newton's law of universal gravitation produces the usual two-body equations of motion

$$\ddot{\mathbf{r}} = -\frac{\mu}{r^2}\mathbf{u} = -\frac{\mu}{r^3}\mathbf{r} \quad (1)$$

where $\mathbf{r} \in \mathbb{R}^3$ is the position of the orbiting body relative to the central body, $r = \|\mathbf{r}\|$ is the range, μ is the central body's gravitational parameter, and

$$\mathbf{u} = \mathbf{r}/r \quad (2)$$

The solution to Eq. (1) produces the classical two-body trajectory equation [23–26]

$$r_i = \frac{h^2/\mu}{1 + e \cos \theta_i} \quad (3)$$

where e is the eccentricity, $h = \|\mathbf{h}\|$ is the magnitude of specific angular momentum, and θ_i is true anomaly. The subscript i has been added to indicate the value of time-dependent variables at time t_i , e.g., $r_i = r(t_i)$ and $\theta_i = \theta(t_i)$. Therefore, the position may be written in the perifocal frame as

$$\mathbf{r}_i = r_i \cos \theta_i \mathbf{p} + r_i \sin \theta_i \mathbf{q} \quad (4)$$

where $\{\mathbf{p}, \mathbf{q}, \mathbf{w}\}$ are usual perifocal frame basis vectors

$$\mathbf{p} = \mathbf{e}/e \quad (5)$$

$$w = \hbar/h \quad (6)$$

$$q = w \times p \quad (7)$$

and where \mathbf{e} is the eccentricity vector ($e = \|\mathbf{e}\|$), which points from the central body to the orbit periapsis.

Now, taking the time derivative of Eq. (4), one arrives at the familiar equation for the satellite velocity in the perifocal frame (an expression generally found in astrodynamics textbooks within the context of converting from orbital elements to position and velocity [23–26]),

$$\mathbf{v}_i = \dot{\mathbf{r}}_i = \frac{\mu}{h} [(-\sin \theta_i) \mathbf{p} + (e + \cos \theta_i) \mathbf{q}] \quad (8)$$

which may be rewritten as

$$\mathbf{v}_i = \frac{\mu}{h} [-\sin \theta_i \mathbf{p} + \cos \theta_i \mathbf{q}] + \frac{\mu}{h} e \mathbf{q} \quad (9)$$

Equation (9) clearly describes a circle of radius μ/h with a center located at $\mu e/hq$. Therefore, defining the hodograph radius R and center \mathbf{c} as

$$R = \frac{\mu}{h} \quad (10)$$

$$\mathbf{c} = \frac{\mu}{\hbar} \mathbf{e} \mathbf{q} = R \mathbf{e} \mathbf{q} = c \mathbf{q} \quad (11)$$

one now arrives at

$$\mathbf{v}_i = R[-\sin \theta_i \mathbf{p} + \cos \theta_i \mathbf{q}] + \mathbf{c} \quad (12)$$

which produces the geometry shown pictorially in Fig. 1.

Furthermore, observe from Eqs. (2) and (4) that

$$\mathbf{u}_i = \cos \theta_i \mathbf{p} + \sin \theta_i \mathbf{q} \quad (13)$$

If \mathbf{u} defines the local vertical, it follows that the local horizontal (positive in the direction of motion) is defined by

$$\mathbf{u}_{\perp_i} = \mathbf{w} \times \mathbf{u}_i = -\sin \theta_i \mathbf{p} + \cos \theta_i \mathbf{q} \quad (14)$$

As a consequence, one immediately sees from Eq. (12) that the line joining the center of the hodograph to the tip of the velocity vector is parallel to the local horizontal. Therefore, substituting Eq. (14) into Eq. (12)

$$v_i = Ru_{\perp_i} + c \quad (15)$$

which yields the following expression for the local horizontal in terms of the velocity and hodograph parameters:

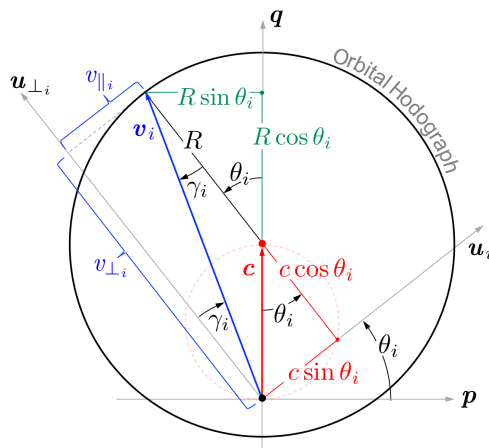


Fig. 1 Illustration of orbital hodograph geometry in the perifocal frame.

$$\mathbf{u}_{\perp_i} = \frac{\mathbf{v}_i - \mathbf{c}}{R} = \frac{\mathbf{v}_i - \mathbf{c}}{\|\mathbf{v}_i - \mathbf{c}\|} \quad (16)$$

Furthermore, recall that the flight path angle (FPA), γ , is the angle between the local horizontal \mathbf{u}_\perp and the velocity vector \mathbf{v} , leading to the geometric relations illustrated in Fig. 1.

The circular structure of the hodograph is only perfectly true for a body perfectly following Keplerian dynamics. This, of course, never happens in practice due to the nonspherical potential of the central body, the presence of other gravitating bodies (i.e., the n -body problem), atmospheric drag, solar radiation pressure, and a host of other perturbing forces. Therefore, just as an actual spacecraft orbit will never perfectly follow a conic section (e.g., circle, ellipse) due to these effects, an actual orbital hodograph will never be a perfect circle. A great deal of literature exists on the perturbation of a spacecraft's trajectory due to non-Keplerian effects, but no such literature (to the knowledge of the authors) presently exists for the orbital hodograph. This is an interesting topic of future work.

III. Constraining the Hodograph with Bearing and Range-Rate Measurements

A. Hodograph Constraints from Central Body Bearing Measurements

Line-of-sight measurements to the central body constrain the orbital plane. A line-of-sight bearing vector from the spacecraft to the planet center points exactly in the $-\mathbf{u}_i$ direction. Therefore, the remainder of this work simply presumes that \mathbf{u}_i is known if central body bearing measurements exist.

Two-body orbital motion is constrained to lie in a plane, such that

$$\mathbf{r}_i \cdot \mathbf{h} = 0 \quad (17)$$

Recall Eqs. (2) and (6) for the spacecraft position and angular momentum,

$$(r_i \mathbf{u}_i) \cdot (h \mathbf{w}) = 0 \rightarrow \mathbf{u}_i^T \mathbf{w} = 0 \quad (18)$$

When multiple ($n \geq 2$) noncolinear bearing measurements are obtained, $\{\mathbf{u}_i\}_{i=1}^n$, they may be used to create a linear system that may be solved for \mathbf{w} in the least-squares sense:

$$\begin{bmatrix} \mathbf{u}_1^T \\ \mathbf{u}_2^T \\ \vdots \\ \mathbf{u}_n^T \end{bmatrix} \mathbf{w} = \mathbf{0}_{n \times 1} \quad (19)$$

This is best achieved using a singular value decomposition (SVD), as discussed at length in [12]. With \mathbf{w} known, the local horizontal may be constructed at each measurement time via the left-hand side of Eq. (14):

$$u_{\perp_i} = w \times u_i \quad (20)$$

B. Hodograph Constraints from Range-Rate Measurements

Assuming a known orbital plane (i.e., \mathbf{w}) and a set of bearing measurements $\{\mathbf{u}_i\}_{i=1}^n$, a corresponding set of range-rate measurements $\{v_{\parallel i}\}_{i=1}^n$ defines the in-plane basis vectors of the perifocal frame (\mathbf{p} and \mathbf{q}) and the center of the orbital hodograph (\mathbf{c}). These quantities may also be used to uniquely solve for the true anomaly at each measurement time, $\{\theta_i\}_{i=1}^n$. This will now be shown.

Begin by decomposing the velocity vector into the components along the local vertical (v_{\parallel_i} along \mathbf{u}_i) and the local horizontal (v_{\perp_i} along \mathbf{u}_{\perp_i}):

$$\mathbf{v}_i = v_{\parallel i} \mathbf{u}_i + v_{\perp i} \mathbf{u}_{\perp i} \quad (21)$$

where it is observed that

$$v_{\parallel i} = \mathbf{v}_i \cdot \mathbf{u}_i \quad \text{and} \quad v_{\perp i} = \mathbf{v}_i \cdot \mathbf{u}_{\perp i} \quad (22)$$

The geometry of Eq. (21) can be seen in Fig. 1 and reveals useful relations for $v_{\parallel i}$ and $v_{\perp i}$ in terms of the hodograph parameters c and R :

$$v_{\parallel i} = c \sin \theta_i \quad \text{and} \quad v_{\perp i} = R + c \cos \theta_i \quad (23)$$

which, as an aside, describes a different circle in the local-vertical/local-horizontal (LVLH) frame.

Equating Eq. (15) and Eq. (21) yields

$$R\mathbf{u}_{\perp i} + \mathbf{c} = v_{\parallel i}\mathbf{u}_i + v_{\perp i}\mathbf{u}_{\perp i} \quad (24)$$

which, after substitution of Eq. (23), may be rearranged as

$$\mathbf{c} = v_{\parallel i}\mathbf{u}_i + (v_{\perp i} - R)\mathbf{u}_{\perp i} = v_{\parallel i}\mathbf{u}_i + c \cos \theta_i \mathbf{u}_{\perp i} \quad (25)$$

This is a geometric result that can be quickly verified from inspection of Fig. 1.

The value of $c \cos \theta_i$ is not yet known. Therefore, remove dependence on the unknown term by taking the cross-product of Eq. (25) with $\mathbf{u}_{\perp i}$ [where $\mathbf{u}_{\perp i}$ is known from Eq. (20)],

$$\mathbf{u}_{\perp i} \times \mathbf{c} = v_{\parallel i}(\mathbf{u}_{\perp i} \times \mathbf{u}_i) + c \cos \theta_i (\mathbf{u}_{\perp i} \times \mathbf{u}_{\perp i}) \quad (26)$$

which may be rewritten using the skew-symmetric cross-product matrix, $\mathbf{a} \times \mathbf{b} = [\mathbf{a} \times] \mathbf{b}$,

$$[\mathbf{u}_{\perp i} \times] \mathbf{c} = -v_{\parallel i} \mathbf{w} \quad (27)$$

When $n \geq 2$ noncolinear measurements are available, this result may be further rewritten as the linear system

$$\begin{bmatrix} [\mathbf{u}_{\perp 1} \times] \\ [\mathbf{u}_{\perp 2} \times] \\ \vdots \\ [\mathbf{u}_{\perp n} \times] \end{bmatrix} \mathbf{c} = \begin{bmatrix} -v_{\parallel 1} \mathbf{w} \\ -v_{\parallel 2} \mathbf{w} \\ \vdots \\ -v_{\parallel n} \mathbf{w} \end{bmatrix} \quad (28)$$

Solving the normal equations directly for \mathbf{c} ,

$$\mathbf{c} = \left(\sum_{i=1}^n [\mathbf{u}_{\perp i} \times]^2 \right)^{-1} \left(- \sum_{i=1}^n v_{\parallel i} [\mathbf{u}_{\perp i} \times] \mathbf{w} \right) \quad (29)$$

which simplifies to

$$\mathbf{c} = - \left(\sum_{i=1}^n [\mathbf{u}_{\perp i} \times]^2 \right)^{-1} \left(\sum_{i=1}^n v_{\parallel i} \mathbf{u}_i \right) \quad (30)$$

Recognizing that the matrix on the left-hand side of Eq. (28) is dependent on the measured bearings, it may sometimes be desirable to solve for \mathbf{c} as a total least squares (TLS) problem [29]. This may be done by rearranging Eq. (28) into

$$\begin{bmatrix} [\mathbf{u}_{\perp 1} \times] & v_{\parallel 1} \mathbf{w} \\ [\mathbf{u}_{\perp 2} \times] & v_{\parallel 2} \mathbf{w} \\ \vdots & \vdots \\ [\mathbf{u}_{\perp n} \times] & v_{\parallel n} \mathbf{w} \end{bmatrix} \begin{bmatrix} \mathbf{c} \\ 1 \end{bmatrix} = \mathbf{0}_{3n \times 1} \quad (31)$$

and finding $[\mathbf{c}^T \ 1]^T$ using the SVD.

With \mathbf{c} found by Eq. (30) [or by the TLS solution to Eq. (31)], building the basis vectors for the perifocal frame is straightforward. For the case where $c \neq 0$, Eq. (11) shows that

$$\mathbf{q} = \frac{\mathbf{c}}{c} \quad (32)$$

and

$$\mathbf{p} = \mathbf{q} \times \mathbf{w} = \frac{\mathbf{c}}{c} \times \mathbf{w} \quad (33)$$

The case where c is identically zero only occurs for circular orbits, where the periapsis is not defined; hence the direction \mathbf{p} is ill-defined. In this case, without loss of generality, the directions of \mathbf{p} may be chosen arbitrarily within the known orbital plane and \mathbf{q} completes the right-handed system.

It is also observed that sufficient information now exists to uniquely define the true anomaly for each of the n measurement times. Direct application of the definition of true anomaly in the perifocal frame yields

$$\cos \theta_i = \mathbf{u}_i \cdot \mathbf{p} \quad (34)$$

$$\sin \theta_i = \mathbf{u}_i \cdot \mathbf{q} \quad (35)$$

which may be used to determine $\theta_i \in [0, 2\pi)$ as

$$\theta_i = \text{atan2}(\sin \theta_i, \cos \theta_i) \quad (36)$$

C. Combining Bearings and Range-Rate Measurements for Initial Orbit Determination

The evaluation of central-body bearing measurements alone produces an estimate of the orbit plane. With the orbit plane known, concurrent range-rate measurements define the location of the hodograph center \mathbf{c} and complete the definition of the perifocal frame $\{\mathbf{p}, \mathbf{q}, \mathbf{w}\}$. Figure 2 illustrates why these measurements alone fail to fully define a unique hodograph. Thus, the only thing that remains to uniquely determine the orbit is to resolve the hodograph radius R ambiguity. A few options are available and are discussed in Sec. IV.

Since the orbit is uniquely defined by \mathbf{c} and R , knowledge of θ_i allows for computation of the position and velocity vectors at each measurement time. Rewrite the trajectory equation from Eq. (3) in terms of hodograph parameters,

$$r_i = \frac{h^2/\mu}{1 + e \cos \theta_i} = \frac{\mu}{R^2 + Rc \cos \theta_i} \quad (37)$$

which, using Eq. (23), recovers by a different means the hodograph relationship developed by Christian in [14]:

$$r_i = \frac{\mu}{Rv_{\perp i}} \quad (38)$$

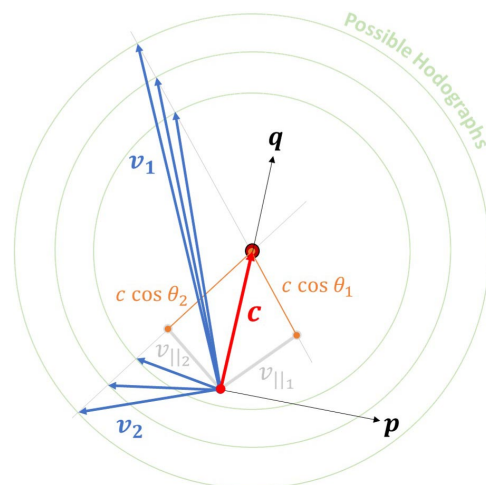


Fig. 2 The hodograph radius is ambiguous when only supplied with bearings and range-rate measurements. Only two ($n = 2$) measurement pairs are shown, but the ambiguity persists for $n \geq 2$.

Table 1 Pseudocode to find position and velocity from a pair of bearing and range-rate measurements

1: procedure $[r_1, r_2, v_1, v_2] = \text{IOD}(u_1, u_2, v_{ 1}, v_{ 2}, \mu)$	
2: compute w	▷ Eq. (19)
3: compute $u_{\perp 1}$ and $u_{\perp 2}$	▷ Eq. (20)
4: compute c	▷ Eq. (30)
5: if $\ c\ > \text{eps}$ then	
6: compute p and q	▷ Eqs. (33) and (32)
7: else	
8: $p \leftarrow u_1$	
9: $q \leftarrow w \times p$	
10: compute θ_1 and θ_2	▷ Eqs. (34–36)
11: compute R	▷ select algorithm from Sec. IV
12: compute r_1 and r_2	▷ Eq. (37)
13: compute r_1 and r_2	▷ Eq. (4)
14: compute v_1 and v_2	▷ Eq. (12)
15: return r_1, r_2, v_1, v_2	▷ position and velocity

Consequently, with the hodograph parameters and perifocal basis vectors known from before, the complete position and velocity vectors may now be constructed using new knowledge of θ_i and r_i through the evaluation of Eqs. (4) and (12). This procedure is summarized in Table 1.

IV. Resolving Hodograph Radius Ambiguity

Given a set of n corresponding bearing measurements $\{u_{||i}\}_{i=1}^n$ and range-rate measurements $\{v_{||i}\}_{i=1}^n$, Sec. III describes the procedure for computing the perifocal frame $\{p, q, w\}$, the true anomaly at each measurement time (θ_1 and θ_2), and hodograph center $c = \mu e/h$. A full IOD solution only requires disambiguation of $R = \mu/h$, meaning that one must find either R or h . Doing this requires additional information, with three such examples discussed in the subsections that follow.

A. Resolving R with Measurement Times

Presuming that the measurement times $\{t_i\}_{i=1}^n$ of the bearing and range-rate measurements are known, the hodograph radius R may be found through analysis of Kepler's equation at two of these times (t_1 and t_2). Of the three methods for resolving R , this is the most practical since time is (comparatively) easy to measure.

Begin by recalling that the orbit semiparameter is given by

$$p = a(1 - e^2) = h^2/\mu \quad (39)$$

such that the mean motion may be written as

$$n = \sqrt{\frac{\mu}{a^3}} = \frac{\mu^2}{h^3} (1 - e^2)^{3/2} \quad (40)$$

or, in terms of only the hodograph parameters c (which is known) and R (which is unknown),

$$n = \frac{1}{\mu} (R^2 - c^2)^{3/2} \quad (41)$$

Likewise, the eccentric anomaly at each measurement time E_i may be written in terms of the known true anomaly θ_i and the hodograph parameters:

$$\sin E_i = \frac{\sqrt{1 - e^2} \sin \theta_i}{1 + e \cos \theta_i} = \frac{\sqrt{R^2 - c^2} \sin \theta_i}{R + c \cos \theta_i} \quad (42)$$

$$\cos E_i = \frac{e + \cos \theta_i}{1 + e \cos \theta_i} = \frac{c + R \cos \theta_i}{R + c \cos \theta_i} \quad (43)$$

With both n and E_i written in terms of the single scalar unknown R , one may find the unique value of R by Kepler's equation. Thus, recall that Kepler's equation states

$$n(t_i - t_p) = M_i = E_i - e \sin E_i \quad (44)$$

where t_p is the time of periapsis passage and M_i is the mean anomaly. Here, both R and t_p are unknown. Fortunately, there are two measurements, so the unknown t_p may be removed by considering the time-of-flight between these two points:

$$n(t_2 - t_1) = 2\pi k + (E_2 - e \sin E_2) - (E_1 - e \sin E_1) \quad (45)$$

where k is the number of periapsis passages that occur between the two measurements. It is presumed that k is known (or can be checked).

Letting $\Delta t = t_2 - t_1$, rewrite Eq. (45) as

$$\begin{aligned} f(R) &= 2\pi k + (E_2 - e \sin E_2) - (E_1 - e \sin E_1) - n\Delta t \\ &= 2\pi k + M_2 - M_1 - n\Delta t \\ &= 0 \end{aligned} \quad (46)$$

where n is from Eq. (41) and E_i is from Eq. (42), both of which are only functions of the scalar unknown R . This is similar in structure to the classic Kepler's problem, though the unknowns are different (R in this problem, θ_2 in classical Kepler's problem).

Considering only closed orbits ($e < 1$), there are easily computable bounds on R . First, from hodograph geometry, the origin must lie within the circle hodograph circle for the orbit to be closed (i.e., $R > c$). Therefore, the minimum value of R is

$$R_{\min} = c \quad (47)$$

The maximum value of R may be computed by not permitting the orbit to intersect the central body's surface. If a central body has a radius r_p (e.g., $r_p \approx 6378$ km for Earth), then the specific angular momentum at periapsis of an orbit grazing the body's surface $h = r_p v_p$. Periapsis corresponds to the point of largest velocity, and may be computed in terms of R and c according to $v_p = R + c$. Therefore, the maximum value of R for a given c may be computed as the planet grazing orbit

$$h = r_p(R + c) = \frac{\mu}{R} \quad (48)$$

which may be written as a quadratic equation in R :

$$R^2 + cR - \frac{\mu}{r_p} = 0 \quad (49)$$

This may be solved for the maximum (unique positive) root to yield the maximum physically permissible value of R :

$$R_{\max} = \frac{1}{2} \left(-c + \sqrt{c^2 + 4\mu/r_p} \right) \quad (50)$$

While Eq. (46) has only one root in the interval (R_{\min}, R_{\max}) , the function $f(R)$ is not monotonically increasing/decreasing with R . The scenario-varying and nonmonotonic shape of $f(R)$ makes this problem ill-suited for direct application of gradient-based algorithms (e.g., Newton-Raphson method). Instead, a robust solution may be quickly found via the bisection method.

1. Finding R with Bisection Method

Since Eq. (46) has only one root on the interval (R_{\min}, R_{\max}) , the intermediate value theorem guarantees that

$$\text{sign}[f(R_{\min})] = -\text{sign}[f(R_{\max})] \quad (51)$$

Therefore, let the initial guess of the lower boundary be $R_{(0)}^- = R_{\min}$ and the initial guess of the upper boundary be $R_{(0)}^+ = R_{\max}$. At each iteration [with iteration number denoted by subscript (ℓ)], compute the midpoint as

$$R_{(\ell)} = \frac{R_{(\ell)}^- + R_{(\ell)}^+}{2} \quad (52)$$

and then update the boundaries according to the conditions

$$\begin{aligned} R_{(\ell+1)}^+ &= R_{(\ell)} \quad \text{if } \text{sign}[f(R_{(\ell)}^+)] = \text{sign}[f(R_{(\ell)})] \\ R_{(\ell+1)}^- &= R_{(\ell)} \quad \text{otherwise} \end{aligned} \quad (53)$$

This procedure is repeated until the difference between $R_{(\ell)}^-$ and $R_{(\ell)}^+$ is small. Note that the midpoint sign check is performed against $R_{(\ell)}^+$ to avoid numerical issues on a finite precision computer that may occur when $R_{\min} \approx 0$. The complete algorithm is summarized in Table 2.

The error at any given iteration of the bisection method is bounded by

$$\epsilon_R = \|R - R_{(\ell)}\| \leq \frac{R_{\max} - R_{\min}}{2^\ell} \quad (54)$$

which describes an iterative procedure with linear convergence. Recalling that the units of R are velocity (e.g., m/s, km/s), one can choose a fixed number of iterations ahead of time and guarantee that the final velocity error is below a specified threshold. Therefore, if the maximum desired velocity error at the conclusion of the bisection algorithm is $\epsilon_v = \epsilon_R$, the maximum number of iterations ℓ_{\max} should be

$$\ell_{\max} = \left\lceil \frac{\ln[(R_{\max} - R_{\min})/\epsilon_v]}{\ln 2} \right\rceil \quad (55)$$

where $\lceil \cdot \rceil$ is the ceiling (round upward) operator.

While the bisection method is very robust, its convergence is slow (only linear). Therefore, once this algorithm gets close to the root, it may be faster to switch to a gradient-based method.

Table 2 Pseudocode to find R via the bisection method when provided measurement times

1: procedure $[R] = \text{FindR_dt_bisection}(c, \theta_1, \theta_2, k, \Delta t, \mu, \epsilon_v)$	
2: $R_{(0)}^- \leftarrow R_{\min}$	▷ Eq. (47)
3: $R_{(0)}^+ \leftarrow R_{\max}$	▷ Eq. (50)
4: compute $E_{1(0)}^+$ and $E_{2(0)}^+$	▷ Eqs. (42) & (43)
5: compute $n_{(0)}^+$	▷ Eq. (41)
6: compute $\text{sign}[f(R_{(0)}^+)]$	▷ Eq. (46)
7: compute ℓ_{\max}	▷ Eq. (55)
8: for $\ell \leftarrow 0$ to $(\ell_{\max} - 1)$ do	
9: compute $R_{(\ell)}$	▷ Eq. (52)
10: compute $E_{1(\ell)}$ and $E_{2(\ell)}$	▷ Eqs. (42) & (43)
11: compute $n_{(\ell)}$	▷ Eq. (41)
12: compute $\text{sign}[f(R_{(\ell)})]$	▷ Eq. (46)
13: if $\text{sign}[f(R_{(\ell)}^+)] = \text{sign}[f(R_{(\ell)})]$ then	
14: $R_{(\ell+1)}^+ \leftarrow R_{(\ell)}$	
15: $E_{1(\ell+1)}^+ \leftarrow E_{1(\ell)}$	
16: $E_{2(\ell+1)}^+ \leftarrow E_{2(\ell)}$	
17: $\text{sign}[f(R_{(\ell+1)}^+)] \leftarrow \text{sign}[f(R_{(\ell)})]$	
18: else	
19: $R_{(\ell+1)}^- \leftarrow R_{(\ell)}$	
20: compute $R_{(\ell+1)}$	▷ Eq. (52)
21: $R \leftarrow R_{(\ell+1)}$	
22: return R	▷ hodograph radius

2. Improving Estimate of R with Newton-Raphson Iteration

Beginning with a good guess of R from the bisection method, the solution for R in Eq. (46) may be refined via Newton-Raphson iteration (which has quadratic convergence). Given the shape of $f(R)$, it should be emphasized that a gradient-based method like this will only work with a very good initial guess of R . It is unlikely that a generic a priori guess of R will be good enough to initialize a Newton-Raphson scheme directly. Therefore, with this warning in mind, take a Taylor series expansion of Eq. (46) and retain terms to first order:

$$f(R) = 0 \approx f(R_{(\ell)}) + f'(R_{(\ell)})(R - R_{(\ell)}) \quad (56)$$

Thus, the iterative solution takes the form of

$$R_{(\ell+1)} = R_{(\ell)} - \frac{f(R_{(\ell)})}{f'(R_{(\ell)})} \quad (57)$$

where (dropping ℓ subscripts for compactness)

$$f'(R) = \frac{\partial f(R)}{\partial R} = \frac{\partial M_2}{\partial R} - \frac{\partial M_1}{\partial R} - \Delta t \frac{\partial n}{\partial R} \quad (58)$$

with contributing partials

$$\frac{\partial M_i}{\partial R} = \left(\frac{c}{R}\right) \left(\frac{c}{R} - \frac{1}{\cos \theta_i}\right) \left(\frac{c \sin \theta_i}{c^2 - R^2} - \frac{\sin \theta_i \cos \theta_i}{R + c \cos \theta_i}\right) + \frac{c \sin \theta_i}{R^2} \quad (59)$$

$$\frac{\partial n}{\partial R} = 3 \frac{R}{\mu} \sqrt{R^2 - c^2} \quad (60)$$

Thus, beginning with a good initial guess for R , Eq. (57) is iterated in the usual manner until the desired convergence is met.

B. Resolving R with Angular Velocity

Consider the situation where, in addition to bearing to the central body and range rate, one was also able to compute the bearing rate (or orbital angular velocity, $\dot{\theta}$). While it is conceivable that a sensor system may be capable of measuring $\dot{\theta}$ directly, it may also be possible to estimate this quantity from sequential bearing measurements. That is, using forward finite differencing,

$$\dot{\theta}_i \approx \arccos\left(\frac{\mathbf{u}(t_i + \Delta t) \cdot \mathbf{u}(t_i)}{\Delta t}\right) \quad (61)$$

Regardless of the source of $\dot{\theta}_i$, presume that one obtains such a measurement corresponding to one of the known true anomalies discussed in Sec. III.B.

Begin by recalling the kinematic relation

$$v_{\perp i} = r_i \dot{\theta}_i \quad (62)$$

which, after substituting for $v_{\perp i}$ from Eq. (23), yields

$$r_i \dot{\theta}_i = c \cos \theta_i + R \quad (63)$$

Next, substitute for r_i using the trajectory equation written in terms of hodograph parameters [see Eq. (37)]:

$$\frac{\mu \dot{\theta}_i}{R^2 + R c \cos \theta_i} = c \cos \theta_i + R \quad (64)$$

This may be rearranged to form a cubic in R :

$$g_i(R) = R^3 + (2c \cos \theta_i)R^2 + (c \cos \theta_i)^2 R - \mu \dot{\theta}_i = 0 \quad (65)$$

$$g_i(R) = R(R + c \cos \theta_i)^2 - \mu \dot{\theta}_i = 0 \quad (66)$$

There will be only one real root corresponding to a valid closed orbit ($R \geq c$). Both checks (realness and $R \geq c$) are necessary in general and can be implemented by construction when solving the cubic equation using well-known techniques [30,31]. The correct root from Eq. (65) represents the fully generic solution for R that is valid for all closed orbits ($e < 1$).

In the case of noncircular orbits where $e \neq 0$ (which is equivalent to $c \neq 0$), it is possible to reduce Eq. (65) to the solution of quadratic. Subtracting Eq. (65) at two different times yields a quadratic equation in R that is easier to solve and is guaranteed to have only one real positive root. That is, find the solution to

$$g_2(R) - g_1(R) = a_2 R^2 + a_1 R + a_0 = 0 \quad (67)$$

where

$$a_2 = 2c(\cos \theta_2 - \cos \theta_1) \quad (68)$$

$$a_1 = c^2(\cos^2 \theta_2 - \cos^2 \theta_1) \quad (69)$$

$$a_0 = \mu(\dot{\theta}_1 - \dot{\theta}_2) \quad (70)$$

As noted above, observe that the simplified quadratic solution for R does not work for a perfectly circular orbit ($e = 0$ and $c = 0$) since

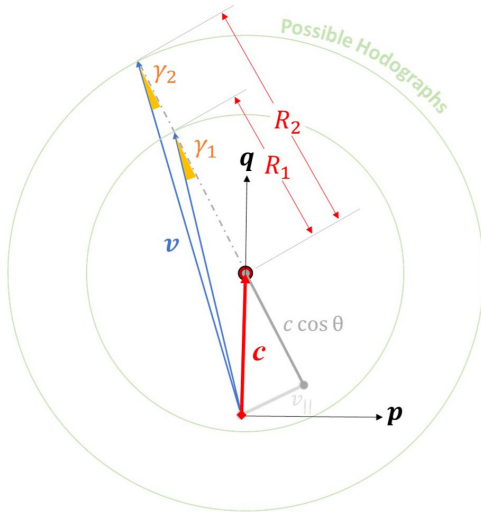


Fig. 3 Specification of the flight path angle γ removes ambiguity in the hodograph radius.

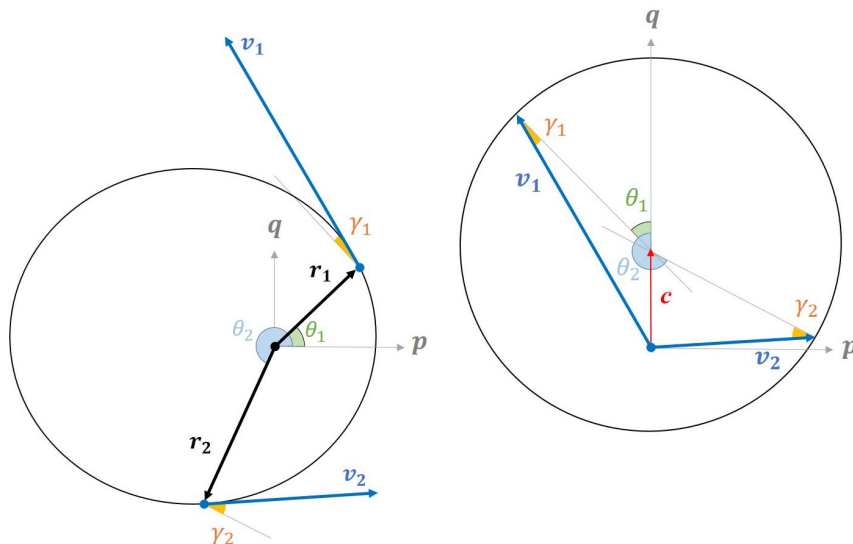


Fig. 4 Orbit (left) and corresponding hodograph (right) for the example scenario used to generate numerical results.

$a_1 = a_2 = a_3 = 0$. The solution in Eq. (67) only works for elliptical orbits.

For a circular orbit ($e = 0$ and $c = 0$), it may appear at first that one must solve the more general cubic equation for R given by Eq. (65). While true, Eq. (65) simplifies greatly for the case of $c = 0$ to yield

$$R^3 = \mu \dot{\theta}_i \quad (71)$$

which may be solved directly for R :

$$R = \sqrt[3]{\mu \dot{\theta}_i} \quad (72)$$

The cube root solution for R is positive since $\mu \dot{\theta}_i > 0$ by construction.

Therefore, in practice, one rarely needs to solve the generic cubic equation from Eq. (65). This general solution is only necessary for elliptical orbits and where only a single measurement of $\dot{\theta}$ is available. If the orbit is elliptical (i.e., if $c \neq 0$) and there are measurements of $\dot{\theta}$ at two times, then one may solve the quadratic equation from Eq. (67). If the orbit is nearly circular (i.e., if $c \approx 0$), then one may solve for R directly by finding the cube root from Eq. (72).

C. Resolving R with the Flight Path Angle

Consider the situation where, in addition to bearing to the central body and range rate, one was also able to measure the flight path angle (FPA), γ_i . Since the LVLH frame is known, the FPA could be inferred by measuring the direction of motion—which is possible in some cases through optical techniques like visual odometry [32–34].

With the location of the center of the hodograph known, consider the definition of the FPA in terms of the LVLH velocity components (see Fig. 1):

$$\tan \gamma_i = \frac{v_{\parallel i}}{v_{\perp i}} \quad (73)$$

Substituting for $v_{\perp i}$ from Eq. (23),

$$\tan \gamma_i = \frac{v_{\parallel i}}{R + c \cos \theta_i} \quad (74)$$

which agrees with the problem geometry illustrated in Fig. 3. The result of Eq. (74) can be rearranged to solve for the unknown R

$$R = \frac{v_{\parallel i}}{\tan \gamma_i} - c \cos \theta_i \quad (75)$$

V. Numerical Results

Both perfect and noisy measurements were simulated to verify that the IOD methods outlined in this paper are realistically implementable and are capable of recovering the true hodograph and true orbit. The example scenario used to assess the performance of these methods sets a spacecraft in a two-body orbit about Earth, with a radius at perigee of 7178.1 km, inclination of 30 deg, argument of periapsis of 70 deg, right ascension of the ascending node (RAAN) of 40 deg, and eccentricity of 0.4. This scenario was similarly used in [12] to assess the performance of velocity-based IOD methods. Figure 4 shows the orbit and corresponding hodograph geometry for the example scenario.

A. Performance with Perfect Measurements

Perfect measurements of range-rate, bearing direction, and measurement-timing were computed for the simulated scenario at true anomalies of 40 and 230 deg (again, see Fig. 4). These measurements were used to perform the IOD procedure outlined in Table 1. The algorithm successfully recovered the true values of c , θ_1 , and θ_2 to within machine precision, as is shown in Table 3. To complete the hodograph fit, the radius ambiguity must be resolved by one of the methods outlined in Sec. IV. Table 4 shows that each method of resolving radius ambiguity was capable of recovering the true hodograph radius, as well as the range and velocity at each measurement time, to within machine precision.

While the angular velocity and FPA-based approaches of resolving R were computed analytically, the measurement-timing approach is iterative. The iteration history of residuals with respect to the true hodograph radius is shown in Table 5 for the Newton-Raphson

Table 5 Newton-Raphson iteration history for hodograph radius error

Iteration number	$\ \delta R\ $ (m/s)
1	1.1737×10^{-5}
2	2.8374×10^{-11}
3	8.8818×10^{-16}

portion of the process outlined in Sec. IV.A. The quadratic convergence of this method allows it to approach machine precision in only three iterations for this scenario.

B. Performance with Measurement Noise

After verifying that the proposed IOD approach is capable of solving for the hodograph (or orbit) parameters given perfect measurements, Gaussian noise was used to perturb these measurements in an effort to assess efficacy on more realistic data. The range-rate, bearing, and timing measurements were assigned noise with reasonable standard deviations of 1 cm/s, 0.01 deg, and 1 ms, respectively. The bearing measurements were perturbed in 3D, resulting in both in-plane and out-of-plane (cross-track) IOD errors.

These perturbed measurements (bearing, range-rate, time) were then supplied to the IOD algorithm to determine the impact of the noise on the final estimates of position and velocity. For this analysis, the measurement-timing approach was used to identify the hodograph radius, since this method is easiest to implement in practice with real sensors. The residuals for spacecraft position at the time of the first measurement were collected over 1000 Monte Carlo runs, and the results are shown in Fig. 5. These data exhibit a maximum range error of 0.1268% with an average range error of 0.0371%.

Error in these results is dominated by the bearing and range-rate errors that produce an estimate of c . To see this, coplot the errors in hodograph parameters c and R , as shown in Fig. 6. When the timing error is 1 ms ($\sigma_t = 0.001$ s), the residuals δc and δR have a correlation near 1. Since c is estimated first and then time is used to estimate R , these results show that errors in finding R are small compared to errors in finding c —such that R inherits the same error as c when the final hodograph is fit. As σ_t increases to 10 s, more noise is introduced

Table 3 IOD-produced estimates of hodograph center and true anomaly are within machine precision when provided perfect measurements

Parameter	Error
$\delta c/c$	3.634×10^{-16}
$\delta \theta_1/\theta_1$	-1.590×10^{-16}
$\delta \theta_2/\theta_2$	-2.212×10^{-16}

Table 4 IOD-produced estimates of hodograph radius, position, and velocity to within machine precision when provided perfect measurements

Radius method	$\delta R/R$	$\delta r_1/r_1$	$\delta r_2/r_2$	$\delta v_1/v_1$	$\delta v_2/v_2$
Measurement-timing	1.938×10^{-16}	-1.252×10^{-16}	-1.424×10^{-16}	-1.424×10^{-16}	2.911×10^{-16}
Angular velocity (at t_1)	1.938×10^{-16}	-1.252×10^{-16}	2.911×10^{-16}	-1.206×10^{-16}	0
Flight path angle	5.814×10^{-16}	-7.513×10^{-16}	-7.120×10^{-16}	4.367×10^{-16}	2.412×10^{-16}

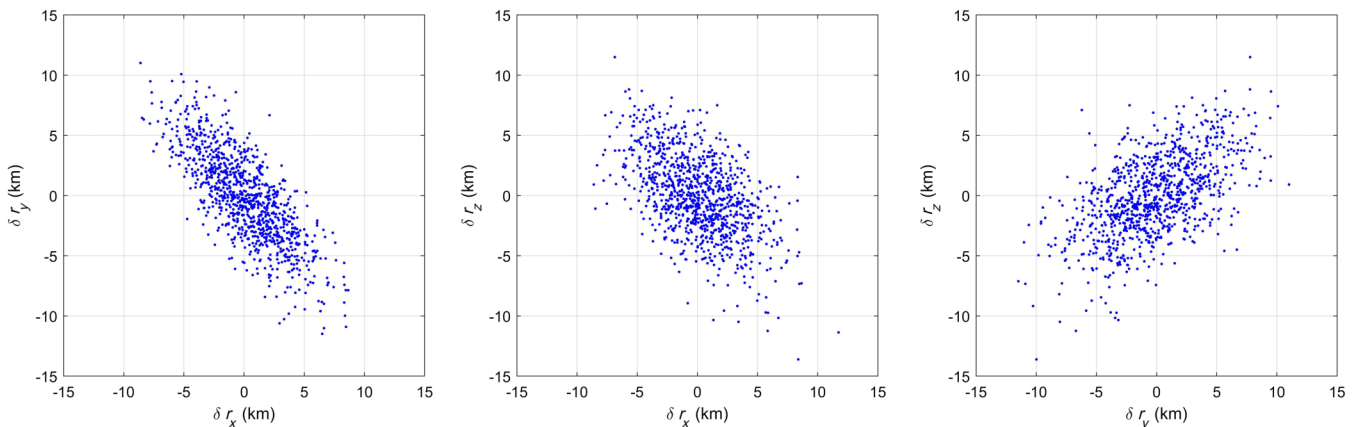


Fig. 5 Errors in position at the time of the first measurement using noisy measurements.

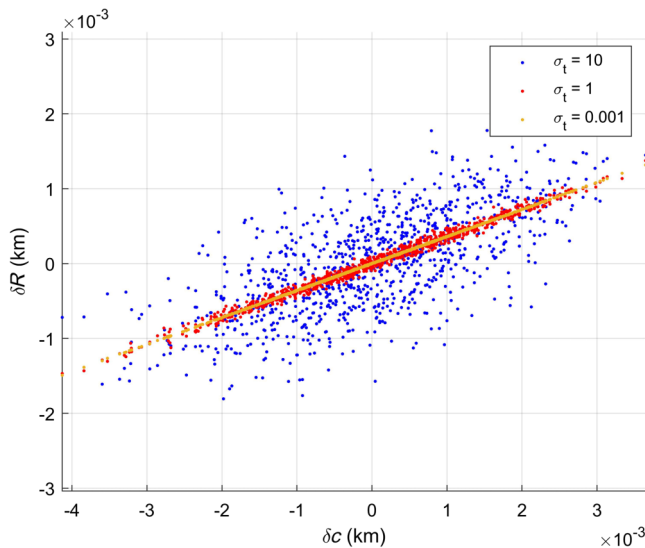


Fig. 6 Increasing the standard deviation for the noise on measurement timing decreases correlation between errors in c and in R .

into the estimate of R and (as expected) the residuals become less correlated.

Though analytic computation of the error covariance is possible in some cases, its development is disproportionately complex when compared to the computation of the IOD solution itself. These difficulties arise from two places. First, the propagation of the bearing measurement errors through the computation of c in Eq. (28) [or Eq. (31)] is a so-called “errors-in-variables” (or TLS) problem. Second, solving for R is generally a root-finding problem, with different equations often being required for different scenarios. While not mathematically difficult, enumeration of the analytic results for each case requires considerable space. A full exploration of these issues is left for future work.

VI. Conclusions

This work introduces a novel IOD approach using measurements of range-rate and bearing to the central body. Under the assumption of two-body orbital mechanics, the solution is developed using the orbital hodograph. The orbital hodograph has long been known to be a perfect circle in this case (a fact that is briefly rederived) and provides an effective tool for intuitive understanding of the problem geometry. Range-rate and bearing measurements alone constrain every element of the orbital hodograph but the radius. Three methods are suggested to resolve the hodograph radius, which depend on observations of 1) measurement times, 2) angular velocity, or 3) flight path angle. Simulation experiments demonstrate that the proposed IOD procedure (for all three options to resolve the hodograph radius ambiguity) is capable of recovering the true solution to within machine precision in the absence of measurement noise. The method is shown to also work in the presence of measurement noise, with performance depending on the amount of sensor noise added.

References

- [1] Laplace, S., “Mémoire sur la Détermination des Orbites des Comètes,” *Mémoires de Mathématique et de Physique*, 1780, pp. 13–72.
- [2] Gauss, C. F., *Theoria Motus Corporum Coelestium in Sectionibus Conicis Solem Ambientum*, F. Perthes and I.H. Besser, Hamburg, Germany, 1809.
- [3] Gibbs, J., “On the Determination of Elliptic Orbits from Three Complete Observations,” *Memoirs of the National Academy of Sciences*, Vol. 4, No. 8, 1889, pp. 79–104.
- [4] Yeomans, D. K., Chodas, P. W., Keesy, M. S., Ostro, S. J., Chandler, J. F., and Shapiro, I. I., “Asteroid and Comet Orbits Using Radar Data,” *Astronomical Journal*, Vol. 103, Jan. 1992, pp. 303–317. <https://doi.org/10.1086/116062>
- [5] Thornton, C., and Border, J., *Radiometric Tracking Techniques for Deep Space Navigation*, Wiley, Hoboken, NJ, 2003.
- [6] Misra, P., and Enge, P., *Global Positioning System: Signals, Measurements, and Performance*, 2nd ed., Ganga-Jamuna Press, Lincoln, MA, 2012.
- [7] Owen, W., “Methods of Optical Navigation,” *AAS/AIAA Space Flight Mechanics Meeting*, American Astronautical Soc. Paper 11-215, San Diego, CA, 2011.
- [8] Christian, J., “Accurate Planetary Limb Localization for Image-Based Spacecraft Navigation,” *Journal of Spacecraft and Rockets*, Vol. 54, No. 3, 2017, pp. 708–730. <https://doi.org/10.2514/1.A33692>
- [9] Sheikh, S., Pines, D., Ray, P., Wood, K., Lovellette, M., and Wolff, M., “Spacecraft Navigation Using X-Ray Pulsars,” *Journal of Guidance, Control, and Dynamics*, Vol. 29, No. 1, 2006, pp. 49–63. <https://doi.org/10.2514/1.13331>
- [10] Escobal, P. R., *Methods of Orbit Determination*, 2nd ed., Robert E. Krieger Publishing Company, Malabar, FL, 1976.
- [11] Tapley, B., Schutz, B., and Born, G., *Statistical Orbit Determination*, Elsevier Academic Press, Amsterdam, 2004. <https://doi.org/10.1016/B978-0-12-683630-1.X5019-X>
- [12] Christian, J., and Hollenberg, C., “Initial Orbit Determination from Three Velocity Vectors,” *Journal of Guidance, Control, and Dynamics*, Vol. 42, No. 4, 2019, pp. 894–899. <https://doi.org/10.2514/1.G003988>
- [13] Hollenberg, C. L., and Christian, J. A., “Geometric Solutions for Problems in Velocity-Based Orbit Determination,” *Journal of the Astronautical Sciences*, Vol. 67, No. 1, 2019, pp. 188–224. <https://doi.org/10.1007/s40295-019-00170-7>
- [14] Christian, J. A., “StarNAV: Autonomous Optical Navigation of a Spacecraft by the Relativistic Perturbation of Starlight,” *Sensors*, Vol. 19, No. 19, 2019, p. 4064. <https://doi.org/10.3390/s19194064>
- [15] Parker, W., Thibeault, R., Quintero, G., and Christian, J., “Guide Star Selection for Spacecraft Navigation with StarNAV,” *43rd Annual AAS Guidance, Navigation and Control Conference*, American Astronautical Soc. Paper 20-123, San Diego, CA, 2020.
- [16] McKee, P., Chrisitan, J., and D’Souza, C., “Analysis of Cislunar Autonomous Navigation with StarNAV and OPNAV,” *43rd Annual AAS Guidance, Navigation and Control Conference*, American Astronautical Soc. Paper 20-041, San Diego, CA, 2020.
- [17] Norton, R., and Wildey, R., “Fundamental Limitations to Optical Doppler Measurements for Space Navigation,” *Proceedings of the IRE*, Vol. 49, No. 11, 1961, pp. 1655–1659. <https://doi.org/10.1109/JRPROC.1961.287769>
- [18] Yim, J., Crassidis, J., and Junkins, J., “Autonomous Navigation of an Interplanetary Spacecraft,” *AAS/AIAA Astrodynamics Specialist Conference*, AIAA Paper 2000-3936, 2000. <https://doi.org/10.2514/6.2000-3936>
- [19] Henderson, T., Pollock, T., Sinclair, A., Theisinger, J., Hurtado, J., and Junkins, J., “Hardware Development and Measurements of Solar Doppler Shift for Spacecraft Orbit Determination,” *AAS/AIAA Astrodynamics Specialist Conference*, American Astronautical Soc. Paper 03-613, San Diego, CA, 2003.
- [20] Sinclair, A., Henderson, T., Hurtado, J., and Junkins, J., “Development of Spacecraft Orbit Determination and Navigation Using Solar Doppler Shift,” *AAS/AIAA Astrodynamics Specialist Conference*, American Astronautical Soc. Paper 03-159, San Diego, CA, 2003.
- [21] Hamilton, W. R., “The Hodograph, or a New Method of Expressing in Symbolical Language the Newtonian Law of Attraction,” *Proceeding of the Royal Irish Academy*, Vol. 3, 1847, pp. 344–353.
- [22] Derbes, D., “Reinventing the Wheel: Hodographic Solutions to the Kepler Problems,” *American Journal of Physics*, Vol. 69, No. 4, 2001, pp. 481–489. <https://doi.org/10.1119/1.1333099>
- [23] Wiesel, W., *Spaceflight Dynamics*, 2nd ed., Irwin/McGraw-Hill, Boston, MA, 1997, pp. 53–54, 66.
- [24] Vallado, D., *Fundamentals of Astrodynamics and Applications*, 3rd ed., Microcosm Press, Hawthorne, CA, 2007, pp. 27–29, 125.
- [25] Curtis, H., *Orbital Mechanics for Engineering Students*, 4th ed., Butterworth-Heinemann, Cambridge, MA, 2020, pp. 67–74, 104.
- [26] Bate, R., Mueller, D., White, J., and Saylor, W., *Fundamentals of Astrodynamics*, 2nd ed., Dover, New York, 2020, pp. 16–17, 58.
- [27] Battin, R. H., *An Introduction to the Mathematics and Methods of Astrodynamics*, rev. ed., AIAA, Reston, VA, 1999, pp. 53–54, 126–127.
- [28] Altman, S., *Orbital Hodograph Analysis*, Vol. 3, American Astronautical Soc., Baltimore, MD, 1965.

- [29] Markovsky, I., and Van Huffel, S., "Overview of Total Least-Squares Methods," *Signal Processing*, Vol. 87, No. 10, 2007, pp. 2283–2302.
<https://doi.org/10.1016/j.sigpro.2007.04.004>
- [30] Cardano, G., *Artis Magnæ, Sive de Regulis Algebraicis Liber Unus* ("Ars Magna"), 1545.
- [31] Zucker, I. J., "The Cubic Equation—A New Look at the Irreducible Case," *Mathematical Gazette*, Vol. 92, No. 524, 2008, pp. 264–268.
<https://doi.org/10.1017/S0025557200183135>
- [32] Nistér, D., Naroditsky, O., and Bergen, J., "Visual Odometry," *Proceedings of the 2004 IEEE Computer Society Conference on Computer Vision and Pattern Recognition (CVPR)*, 2004.
<https://doi.org/10.1109/CVPR.2004.1315094>
- [33] Scaramuzza, D., and Fraundorfer, F., "Visual Odometry Part I: The First 30 Years and Fundamentals," *IEEE Robotics & Automation Magazine*, Vol. 18, No. 4, 2011, pp. 80–92.
<https://doi.org/10.1109/MRA.2011.943233>
- [34] Christian, J. A., Hong, L., McKee, P., Christensen, R., and Crain, T. P., "Image-Based Lunar Terrain Relative Navigation Without a Map: Measurements," *Journal of Spacecraft and Rockets* (in press).
<https://doi.org/10.2514/1.A34875>